

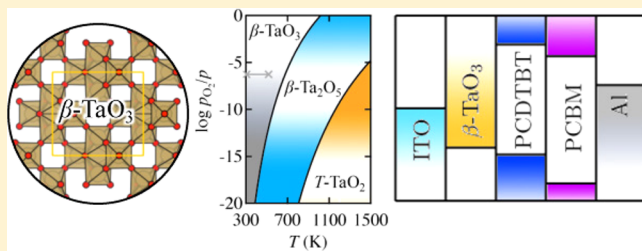
## Over-Stoichiometry in Heavy Metal Oxides: The Case of Iono-Covalent Tantalum Trioxides

Yun-Jae Lee,<sup>ID</sup> Taehun Lee,<sup>ID</sup> and Aloysius Soon\*<sup>ID</sup>

Department of Materials Science and Engineering, Yonsei University, Seoul 03722, Korea

Supporting Information

**ABSTRACT:** Oxides of tantalum (common examples including  $\text{TaO}$ ,  $\text{TaO}_2$ , and  $\text{Ta}_2\text{O}_5$ ) are key oxide materials for modern electronic devices, such as dynamic random-access memory and field effect transistors. Of late, new forms of stable tantalum oxides have been proposed as two-dimensional nanosheet structures with a nonconventional stoichiometry of  $\text{TaO}_3$  via soft-chemical delamination of  $\text{RbTaO}_3$ . However, not much is known about the elusive nanosheet-structured  $\text{TaO}_3$ , unlike other closely related common trioxides of W and Mo. In this work, using first-principles density functional theory calculations, we have studied various  $\text{TaO}_3$  structures as inspired from previous theoretical and experimental studies and discuss their properties with respect to the more conventional oxide of tantalum,  $\text{Ta}_2\text{O}_5$ . We have calculated their thermodynamics and lattice properties and have found a new stable-layered  $\beta\text{-TaO}_3$  and its exfoliated monolayer phase ( $\beta'$ ). By further analyzing their electronic structures, we discuss the mixed iono-covalent bonding characteristics in the  $\text{TaO}_3$  phases, challenging the conventional formal oxidation state model for metal oxides. Finally, we propose how these new  $\text{TaO}_3$  oxide materials may be potentially useful in photodevice applications.



### 1. INTRODUCTION

Transition metal oxides (TMO) are well-known for their ability to adopt multiple metal oxidation states (i.e., partial filling of the d states), depending primarily on their bonding environment and compound stoichiometry. This multivalency governs the overall functionality of the oxide material, e.g., in its wide use in clean energy technologies and advanced (opto)-electronics.<sup>1</sup>

The recent advances in the ability to modify and control the dimensionality of bulk oxides (e.g., via chemical exfoliation) have led to a new class of low-dimensional oxide nanomaterials which show very distinct structural and electronic properties from their parent bulk oxide materials.<sup>2,3</sup>

These new low-dimensional oxide nanomaterials may then be stacked with other known layered nanomaterials, such as transition metal dichalcogenide monolayers (TMDC), graphene, and hexagonal boron nitride (*h*-BN), to make two-dimensional (2D) heterostructures for various key technological applications, for example, for photoconducting cells, *p*–*n* junctions, and field effect transistors.<sup>4</sup>

Despite the existence of these so-called low-dimensional “nanosheet oxides” (e.g., in few-atom-layered Ti, Nb, Mn, and Mo oxides), the design and discovery of new nanosheet oxides must be accelerated to meet their ever increasing demand as novel nano building blocks for miniaturized complex devices.<sup>5</sup>

Bulk oxides of tantalum (common examples including  $\text{TaO}$ ,  $\text{TaO}_2$ , and  $\text{Ta}_2\text{O}_5$ )<sup>6</sup> are known for their niche applications in modern nanoelectronics.<sup>7–9</sup> For instance, various polymorphic phases of  $\text{Ta}_2\text{O}_5$  have been used in capacitors for dynamic

random-access memory (DRAM), field effect transistors, and coating materials.<sup>7</sup>

Aside from the more common valencies listed above, a less common and elusive oxide of tantalum (with the chemical stoichiometry of  $\text{TaO}_3$ ) was synthesized by the group of T. Sasaki and co-workers,<sup>10,11</sup> where low-dimensional structures of  $\text{TaO}_3$  were proposed and showed great promise as excellent electrolyte coating materials for solid battery applications. Unfortunately, insufficient structural information on this two-dimensional  $\text{TaO}_3$  was reported in their work. Unlike for the case of  $\text{Ta}_2\text{O}_5$ <sup>12</sup> and other closely related trioxides of W<sup>13,14</sup> and Mo,<sup>15</sup> polymorphic expressions in this metastable  $\text{TaO}_3$  have not yet been explored.

In a more recent theoretical work by Ravi and co-workers,<sup>16</sup> inspired by the cubic  $\text{ReO}_3$ -type structure of  $\text{TaO}_2\text{F}$ ,<sup>17</sup> they attempted to study this hypothetical geometry of  $\text{TaO}_3$  with density functional theory (DFT) calculations within the semilocal approximation to the exchange-correlation (*xc*) functional. There, they found that this hypothetical structure of  $\text{TaO}_3$  is both energetically and dynamically (and elastically) stable and presents self-doped p-type conductivity (according to the Zaanen–Sawatzky–Allen scheme). Here, we question the propriety and accuracy of this work, given that neither the spin state of this metastable oxide nor the underestimation due to the semilocal *xc* functional used was discussed.<sup>16</sup>

Received: March 6, 2018

Published: April 30, 2018

In this work, we analyze the thermodynamics and lattice properties of this less common oxide of tantalum, TaO<sub>3</sub>, using first-principles spin-polarized DFT calculations, and we discuss these structures with respect to the more common oxide of tantalum, Ta<sub>2</sub>O<sub>5</sub>. We then report the electronic properties of these new TaO<sub>3</sub> polymorphs (as calculated using the more accurate hybrid DFT *xc* functional) with their potential use in polymer solar cells (PSCs) in mind.

## 2. METHODOLOGY

Spin-polarized DFT calculations in this work are performed using periodic boundary conditions, employing the projector augmented-wave (PAW)<sup>18,19</sup> method as implemented in the Vienna *Ab initio* Simulation Package (VASP) code.<sup>20,21</sup> The Kohn–Sham orbitals are expanded using a plane-wave basis set with a kinetic cutoff energy of 500 eV.

A  $\Gamma$ -centered k-point mesh with a spacing of 0.2 Å<sup>-1</sup> is used to sample the Brillouin zone, which corresponds to 8 × 8 × 8, 4 × 4 × 6, and 4 × 4 × 1 k-point grids for the  $\alpha$ ,  $\beta$ , and  $\beta'$  phases of TaO<sub>3</sub>, respectively. The corresponding k-point grid used for  $\beta$ -Ta<sub>2</sub>O<sub>5</sub> is 9 × 9 × 5.

When addressing the energetics and lattice properties of various tantalum oxide structures, we tested a few semilocal approximations to the *xc* functional, namely, the Perdew, Burke, and Ernzerhof (PBE)<sup>22</sup> and its revised form for solids (PBEsol),<sup>23</sup> as well as the self-consistent van der Waals (vdW) corrected *xc* functional, optB88.<sup>24,25</sup> The latter (optB88) is found to provide the most balanced description for the energetics and lattice properties of TaO<sub>3</sub>.

To overcome the well-known deficiencies in these semilocal *xc* functionals when calculating the electronic band structure, the hybrid DFT *xc* functional from Heyd, Scuseria, and Ernzerhof (HSE06)<sup>26,27</sup> is employed. Here, a reduced k-point grid is used to lower the computational cost (i.e., 4 × 4 × 4 for  $\alpha$ -TaO<sub>3</sub>, 2 × 2 × 3 for  $\beta$ -TaO<sub>3</sub>, and 2 × 2 × 1 for  $\beta'$ -TaO<sub>3</sub>), while the 0.2 Å<sup>-1</sup> spaced k-point grid is kept when calculating the optical responses (as described in the Supporting Information).

To assess the energetic stability of the various polymorphic phases of TaO<sub>3</sub> and  $\beta$ -Ta<sub>2</sub>O<sub>5</sub>, we calculate their formation energies ( $\Delta H_{\text{Ta}_x\text{O}_y}^f$ , in eV/atom) with respect to the bulk bcc phase of Ta and the O<sub>2</sub> molecule as follows

$$\Delta H_{\text{Ta}_x\text{O}_y}^f = \frac{1}{N_{\text{Ta}} + N_{\text{O}}} \left( E_{\text{Ta}_x\text{O}_y} - N_{\text{Ta}} E_{\text{Ta}}^{\text{bulk}} - \frac{N_{\text{O}}}{2} E_{\text{O}_2}^{\text{mle}} \right) \quad (1)$$

where  $N_{\text{Ta}}$ ,  $N_{\text{O}}$ ,  $E_{\text{Ta}_x\text{O}_y}$ ,  $E_{\text{Ta}}^{\text{bulk}}$ , and  $E_{\text{O}_2}^{\text{mle}}$  are the number of tantalum and oxygen atoms, the total energy of bulk tantalum oxide, the total energy of bulk tantalum, and the total energy of the oxygen molecule, respectively.

Next, the Gibbs free energy of bulk formation as a function of the chemical potential of oxygen,  $\Delta G^f$ , is then defined as

$$\Delta G^f = \frac{1}{N_{\text{Ta}}} \left( E_{\text{Ta}_x\text{O}_y} - N_{\text{Ta}} E_{\text{Ta}}^{\text{bulk}} - \frac{N_{\text{O}}}{2} E_{\text{O}_2}^{\text{mle}} - N_{\text{O}} \Delta \mu_{\text{O}} \right) \quad (2)$$

Here, the change in the chemical potential of oxygen,  $\Delta \mu_{\text{O}}$ , is taken as the chemical potential of oxygen ( $\mu_{\text{O}}$ ) calculated with respect to half the total energy of the O<sub>2</sub> molecule, i.e.,  $\Delta \mu_{\text{O}} = \mu_{\text{O}} - \frac{1}{2} E_{\text{O}_2}^{\text{mle}}$ . To correct for the known large error in the calculated O<sub>2</sub> binding energy within the semilocal approximation to the *xc* functional, the experimental binding energy of the O<sub>2</sub> molecule without a zero-point energy (5.22 eV) is used, following ref 28.

Lattice dynamics calculations have been performed to address the dynamic stability of the  $\alpha$ ,  $\beta$ , and  $\beta'$  phases of TaO<sub>3</sub>. Using a 2 × 2 × 2 supercell for  $\alpha$ -TaO<sub>3</sub> and  $\beta$ -TaO<sub>3</sub> (and a 2 × 2 × 1 supercell for  $\beta'$ -TaO<sub>3</sub>) and adopting the finite-difference approach (as implemented in the VASP code), we calculate the force constants and compute the phonon dispersion plots using those DFT-derived force constants with the PHONOPY code.<sup>29</sup> Details of this implementation of the

PHONOPY code can be found elsewhere.<sup>29</sup> Likewise, the second-order elastic constants,  $C_{ij}$ , for each TaO<sub>3</sub> structure are tested against the Born(-Huang) elastic stability criteria, as detailed in ref 30.

To examine the chemical characteristics of the Ta–O bonds in TaO<sub>3</sub>, we compute the electron localization function (ELF(r)), difference charge density ( $\Delta\rho(\mathbf{r})$ ), and Bader charges using the hybrid HSE06 *xc* functional. Formally, ELF(r) simply takes the form of

$$\text{ELF}(\mathbf{r}) = \frac{1}{1 + \left( \frac{D(\mathbf{r})}{D_h(\mathbf{r})} \right)^2} \quad (3)$$

where  $D(\mathbf{r})$  and  $D_h(\mathbf{r})$  are the measurement of the electron localization for the system in question and that for the uniform electron gas, respectively.<sup>31</sup> Further,  $\Delta\rho(\mathbf{r})$  is then taken as

$$\Delta\rho(\mathbf{r}) = \rho_{\text{TaO}_3}^T(\mathbf{r}) - \rho_{\text{TaO}_3}^U(\mathbf{r}) - \rho_{\text{TaO}_3}^L(\mathbf{r}) \quad (4)$$

where  $\rho_{\text{TaO}_3}^T(\mathbf{r})$  is the total electron charge density of a doubled unit cell through the *c*-axis and  $\rho_{\text{TaO}_3}^U(\mathbf{r})$  and  $\rho_{\text{TaO}_3}^L(\mathbf{r})$  are those for the upper and lower TaO<sub>3</sub> layers in the doubled supercell, respectively.

To align the conduction ( $\epsilon_{\text{CMB}}$ ) and valence ( $\epsilon_{\text{VMB}}$ ) band edges of various TaO<sub>3</sub> polymorphic phases and  $\beta$ -Ta<sub>2</sub>O<sub>5</sub>, we first calculate the O 1s core state for the different TaO<sub>3</sub> structures and  $\beta$ -Ta<sub>2</sub>O<sub>5</sub> using the HSE06 *xc* functional. Next, to align the band edges to the absolute vacuum level, we determine the vacuum level ( $V_{\text{vac}}$ ) of the 2D  $\beta'$ -TaO<sub>3</sub> nanosheet and use that as a reference. Considering the O 1s core state of TaO<sub>3</sub> and Ta<sub>2</sub>O<sub>5</sub> and  $V_{\text{vac}}$  of  $\beta'$ -TaO<sub>3</sub>, we then determine the ionization potential (IP) and electron affinity (EA) (as defined from  $\epsilon_{\text{CMB}}$  and  $\epsilon_{\text{VMB}}$ ). More details can be found in refs 32 and 33.

## 3. RESULTS AND DISCUSSION

**3.1. Atomic Structures.** The successful exfoliation of layered oxide nanostructures with dissimilar charge states and controllable physicochemical properties, such as in MnO<sub>2</sub>, MoO<sub>3</sub>, and TiO<sub>2</sub>, has promoted further research and studies of low-dimensional 2D nanosheet oxides.<sup>2,5</sup> In 2007, the group of T. Sasaki and co-workers prepared the over-stoichiometric crystalline TaO<sub>3</sub> nanosheet structure, possessing a layered geometry unlike the conventional tantalum oxide phases (TaO, TaO<sub>2</sub>, and Ta<sub>2</sub>O<sub>5</sub>) by chemically removing the intercalated Rb cation from layered RbTaO<sub>3</sub>.<sup>10</sup> Three years later in 2010, the same group then successfully synthesized multilayered TaO<sub>3</sub> by depositing successive TaO<sub>3</sub> nanosheets on a polymeric substrate.<sup>34</sup>

Inspired by the group of T. Sasaki, we investigate the physicochemical properties of these less common layered TaO<sub>3</sub> phases. First, to mimic the experiments, we build and construct the TaO<sub>3</sub> structure by removing the Rb cations from the experimentally reported RbTaO<sub>3</sub> structure.<sup>35</sup> The optimized, layered TaO<sub>3</sub> geometry is shown in Figures 1(b) and 1(c), denoted as the  $\beta$ -phase and with a monoclinic crystal structure with the C2/m space group. The unit cell has 8 Ta and 24 O atoms with two units of 4 edge-shared distorted TaO<sub>6</sub> octahedrons which possess a severe off-centered distortion of the central Ta atom in the TaO<sub>6</sub> building component.

The unique stacking sequence of this layered  $\beta$ -TaO<sub>3</sub> along the *c*-axis brings about the formation of two porous channels, the rectangular (denoted as A in Figure 1(b)) and the parallelogrammatic (denoted as B in Figure 1(b)) channels. These channels have been proposed as promising ionic conducting channels for potential applications in solid state lithium batteries.<sup>11</sup>

To generate the atomic geometry of the experimentally suggested single TaO<sub>3</sub> nanosheet, one monolayer (ML) layer unit composed of 3 edge-shared TaO<sub>6</sub> (denoted as  $\beta'$ -TaO<sub>3</sub>) in

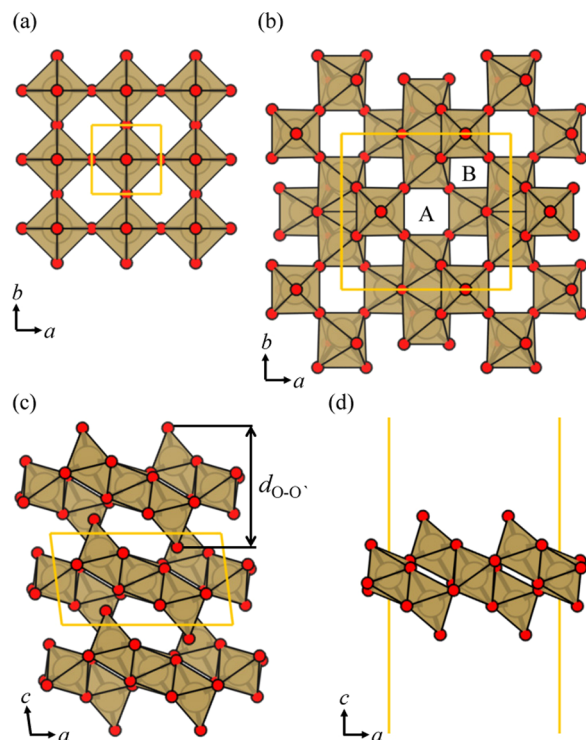


**Figure 1.** Crystal structures and atomic geometries of (a) cubic  $\alpha$ -TaO<sub>3</sub>, layered  $\beta$ -TaO<sub>3</sub> from its (b) top view and (c) side view, and (d) nanosheet  $\beta'$ -TaO<sub>3</sub>. The O and Ta atoms are denoted by the red and khaki colored spheres, respectively. The connecting polyhedrons are shown in khaki, and the unit cells are depicted with yellow lines.

the vertical direction ( $c$ -axis) is exfoliated from stacked  $\beta$ -TaO<sub>3</sub>, as shown in Figure 1(c). The optimized  $\beta'$ -TaO<sub>3</sub> structure has an outermost oxygen–oxygen interlayer vertical distance,  $d_{\text{O}-\text{O}'}$ , of 6.95 Å. When we compare this value to the experimental value (0.66 nm or 6.6 Å) as measured by atomic force microscopy,<sup>10</sup> it shows a rather small difference (approximately 5%) which may have originated from the interaction between TaO<sub>3</sub> and the silicon substrate used in the experiments.<sup>10</sup>

Following a recent computational study,<sup>16</sup> it has been reported that the cubic ReO<sub>3</sub>-type TaO<sub>3</sub> structure (here, denoted as  $\alpha$ -TaO<sub>3</sub> and shown in Figure 1(a)) is deemed thermodynamically stable.  $\alpha$ -TaO<sub>3</sub> yields a negative formation energy as calculated using the GGA-PBE  $xc$  functional. In this work, the  $\alpha$  phase has been included to compare the thermodynamic and lattice stability of nanosheet structures. Our computed lattice parameter of  $\alpha$ -TaO<sub>3</sub> of 3.95 Å shows good agreement with the previous study.<sup>16</sup>

**3.2. Thermodynamics.** Using eq 1, we calculated the enthalpy of formation ( $\Delta H^{\text{f}}$ ) for the various structures of TaO<sub>3</sub> and list them in Table 1. In our calculation results,  $\beta$ -TaO<sub>3</sub> is found to have the lowest  $\Delta H^{\text{f}}$  at −2.85 eV/atom, which results in it being slightly thermodynamically more stable than  $\alpha$ -TaO<sub>3</sub>.

**Table 1.** Lattice Parameters,<sup>a</sup> Energetics,<sup>b</sup> and Spin Magnetic Moments<sup>c</sup> for the Various TaO<sub>3</sub> Polyphases<sup>d</sup>

	$a$	$b$	$c$	$\alpha$	$\beta$	$\gamma$	$d_{\text{O}-\text{O}'}$	space group	$\Delta H^{\text{f}}$	$\mu_s$
$\alpha$ -TaO <sub>3</sub>	3.95	3.95	3.95	90	90	90		<i>Pm3m</i>	−2.81	0.21
$\beta$ -TaO <sub>3</sub>	9.72	8.91	5.13	90	94.3	90	6.91	<i>C2/m</i>	−2.85	
$\beta'$ -TaO <sub>3</sub>	9.77	8.57	26.73	90	90	90	6.95		−2.59	0.20

<sup>a</sup>Values for  $a$ ,  $b$ ,  $c$ , and  $d_{\text{O}-\text{O}'}$  in angstroms (Å) and  $\alpha$ ,  $\beta$ , and  $\gamma$  in degrees (°). <sup>b</sup> $\Delta H^{\text{f}}$  in eV/atom. <sup>c</sup> $\mu_s$  in  $\mu_B$ /atom. <sup>d</sup>All results presented here are calculated using the optB88  $xc$  functional.

(−2.81 eV/atom). Here,  $\beta'$ -TaO<sub>3</sub> shows the highest  $\Delta H^{\text{f}}$  of −2.59 eV/atom among TaO<sub>3</sub> structures. We attribute this difference of approximately 0.2 eV/atom, when compared to  $\beta$ -TaO<sub>3</sub>, to the energy cost from structurally exfoliating  $\beta$ -TaO<sub>3</sub> to  $\beta'$ -TaO<sub>3</sub>. Further analysis from the viewpoint of electronic structure for these structures will be discussed below.

To afford a thermodynamic assessment of the relative stabilities among the various tantalum oxides of different chemical stoichiometry, i.e., between  $\beta$ -TaO<sub>3</sub> and other TaO, TaO<sub>2</sub>, and Ta<sub>2</sub>O<sub>5</sub>, their Gibbs free energy of formation ( $\Delta G^{\text{f}}$ ) is calculated (cf. eq 2) and plotted in Figure 2(a) as a function of the change of oxygen chemical potential ( $\Delta \mu_O$ ).

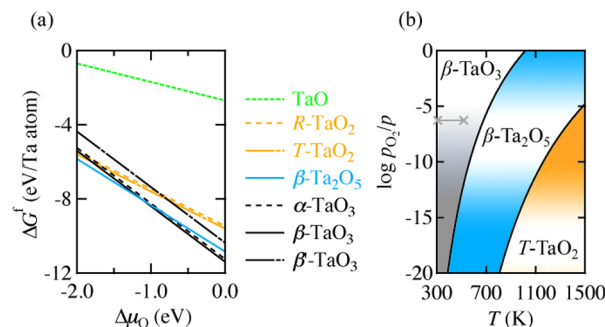


**Figure 2.** (a) Gibbs free energy of formation ( $\Delta G^{\text{f}}$ ) for TaO, R-TaO<sub>2</sub>, T-TaO<sub>2</sub>,  $\beta$ -Ta<sub>2</sub>O<sub>5</sub>, and  $\beta$ -TaO<sub>3</sub> as a function of the change of oxygen chemical potential ( $\Delta \mu_O$ ). (b) Bulk phase diagram of Ta–O compounds as a function of temperature and pressure of the oxygen gas. Detailed atomic geometries and computed  $\Delta H^{\text{f}}$  values for the oxides are depicted in Figure S1 and Tables S1 and S2 of the SI.

Here, we choose the representative thermodynamic structures for each Ta–O stoichiometry: TaO (in the rocksalt structure), R-TaO<sub>2</sub> (in the rutile structure), triclinic T-TaO<sub>2</sub> and  $\beta$ -Ta<sub>2</sub>O<sub>5</sub> (with a space group *Pmm*).<sup>12,36,37</sup> Specifically for the case of Ta<sub>2</sub>O<sub>5</sub>, the energetics and structural properties of its polymorphs are still actively debated and researched.<sup>12,38</sup> Given the complex local atomic distortions between the Ta and O atoms found in Ta<sub>2</sub>O<sub>5</sub>, it is still not conclusive which polymorphic phase of Ta<sub>2</sub>O<sub>5</sub> is the actual ground state structure.

Thus, in this work where Ta<sub>2</sub>O<sub>5</sub> is used only as a reference, we have chosen the more well-studied  $\beta$ -Ta<sub>2</sub>O<sub>5</sub> as a representative polymorph for Ta<sub>2</sub>O<sub>5</sub>.<sup>12</sup> The atomic geometries of the various tantalum oxides of different chemical stoichiometry are shown in Figure S1, and their enthalpies of formation are listed in Table S1. Referring to Figure 2(a), under oxygen-lean conditions, T-TaO<sub>2</sub> is most stable until  $\Delta \mu_O = -2.48$  eV. Under more oxidizing conditions,  $\beta$ -Ta<sub>2</sub>O<sub>5</sub> is the most favored phase when  $\Delta \mu_O$  is between −2.48 and −1.11 eV. Beyond  $\Delta \mu_O = -1.11$  eV,  $\beta$ -TaO<sub>3</sub> is then the thermodynamically most preferred phase. Within our considered range of  $\Delta \mu_O$ , rocksalt TaO is only metastable.

Revisiting previous experiments mentioned above, the group of T. Sasaki prepared  $\text{TaO}_3$  using a solution-based synthesis method.<sup>10,11,34</sup> However, there have been several recent reports where vapor-based (i.e., gas phase reactions) preparation methods for  $\text{Ta}_2\text{O}_{5+x}$  have yielded O/Ta ratios ranging from 2.8 to 3.3. They have further characterized their  $\text{Ta}_2\text{O}_{5+x}$  samples via X-ray photoemission spectroscopy (XPS) and have found the O 1s core levels at 529.7 eV as compared to that of  $\text{Ta}_2\text{O}_5$ . More specifically, the measurements have been conducted under 2.4 mTorr of oxygen pressure (until 473.15 K was reached)<sup>9</sup> as well as in a pure  $\text{O}_2$  environment at room temperature using the physical vapor deposition of Ta.<sup>39</sup>

Using our calculated  $\Delta G^f(\Delta\mu_{\text{O}})$  values and by assuming that oxygen behaves as an ideal gas at the  $p$  (pressure) and  $T$  (temperature) of interest, we present the theoretically derived ( $p$ ,  $T$ ) phase diagram for the Ta–O system in Figure 2(b). The ( $p$ ,  $T$ ) region where the experimentally observable overstoichiometric oxides of tantalum were reported<sup>9,39</sup> is denoted by gray markers and solid lines, and this nicely coincides with the stability region of  $\beta\text{-TaO}_3$ . We then argue that the experimentally synthesized “ $\text{Ta}_2\text{O}_{5+x}$ ” sample under 400 K and oxygen-rich conditions could well be closely related to  $\beta\text{-TaO}_3$  based on our thermodynamics analysis. Notably,  $\beta\text{-Ta}_2\text{O}_5$  is the most dominant phase over the range of oxygen pressures and temperatures, which is in good agreement with the previous experimental Ta–O phase diagram.<sup>40</sup>

**3.3. Structural Stability.** To determine the elastic stability for each  $\text{TaO}_3$  structure, we calculate the zero-pressure elastic constants ( $C_{ij}$ ) and find that they all satisfy the Born stability criteria<sup>30</sup> and that they all are elastically stable. The Born stability relations are detailed in the Supporting Information, and our calculated  $C_{ij}$  values for each  $\text{TaO}_3$  structure are listed in Table S3. We further examine their dynamical stabilities by computing their phonon dispersions via a finite-difference supercell force constant method. The phonon band structures and densities of state for  $\alpha$ -,  $\beta$ -, and  $\beta'$ - $\text{TaO}_3$  are shown in Figure S2 (where the longitudinal optical–transverse optical (LO–TO) splitting is explicitly included). We find  $\alpha\text{-TaO}_3$  to be dynamically stable with no imaginary (i.e., negative) frequency modes, agreeing well with the overall phonon dispersion plot in ref 16.

For  $\beta\text{-TaO}_3$ , a very minute negative frequency mode ( $-0.37$  THz or  $-1.53$  meV) is found between the A and  $\Gamma$  points (see Figure S2(b)). We attribute this negligible numerical noise to the size of the supercell used and the choice of  $xc$  functionals<sup>41,42</sup> which can sensitively contribute to the occurrence of unphysical negative modes. We have also further cross-checked this with a density functional perturbation theory (DFPT)<sup>43</sup> calculation (as implemented in the Quantum ESPRESSO package,<sup>44,45</sup> see Figure S3) where no imaginary frequency modes along the high symmetry points are found. Thus, we reason that  $\beta\text{-TaO}_3$  is dynamically stable within the accuracy of our calculations.

In the case of the nanosheet-structured  $\beta'\text{-TaO}_3$ , we find a marginally larger negative frequency mode at the  $\Gamma$  point (of about  $-1.04$  THz or  $-4.30$  meV, see Figure S2(c)). Upon closer inspection, this negative frequency mode originates from an out-of-plane phonon instability that is rather commonly observed in other 2D single-layered nanostructures.<sup>46,47</sup> We argue that though  $\beta'\text{-TaO}_3$  may be dynamically unstable as a free-standing nanosheet, an appropriate choice of growth supports and/or substrates (e.g., silicon<sup>10</sup>) can assist in the stabilization of  $\beta'\text{-TaO}_3$ .

**3.4. Electronic Structure.** Now, we turn our attention to the fundamental electronic properties of  $\text{TaO}_3$ . To obtain a more accurate description of its electronic structure, spin unrestricted HSE06-computed electronic band structures and the corresponding projected densities of states (PDOS) are plotted in Figure 3 for various  $\text{TaO}_3$  polyphases. As compared

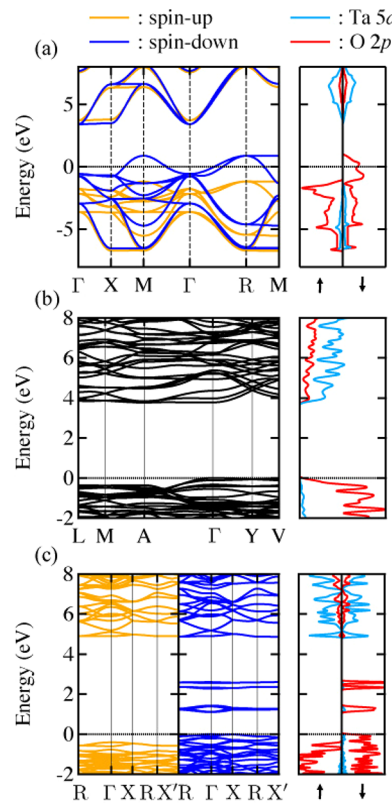


**Figure 3.** (Left) Spin-resolved electronic band structures and (right) corresponding projected densities of state (PDOS) of Ta 5d and O 2p states for (a)  $\alpha\text{-TaO}_3$ , (b)  $\beta\text{-TaO}_3$ , and (c)  $\beta'\text{-TaO}_3$ . The Fermi energy ( $e_{\text{VMB}}$ ) is aligned to a zero value. The up-spin and down-spin states are denoted by the up and down arrows, respectively.

to the closely related  $\text{WO}_3$  polymorphs,<sup>13</sup> the O 2p and Ta 5d states in  $\text{TaO}_3$  polyphases are dominant at the valence and conduction band edges, respectively. This is in contrast to yet another closely related heavy metal trioxide,  $\text{MoO}_3$ .<sup>15</sup>

Unlike in ref 16, we find that  $\alpha\text{-TaO}_3$  expresses a magnetic spin moment of  $0.21 \mu_{\text{B}}/\text{atom}$ , and its spin-resolved band structure and PDOS are plotted in Figure 3(a). For its up-spin state, a large indirect band gap energy ( $E_g$ ) of  $4.95$  eV ( $4.86$  eV) from M to  $\Gamma$  (R to  $\Gamma$ ) k-point is found, whereas for the down-spin case, partially filled O 2p states result in a semimetallic, self-doped p-type conductivity that was previously suggested in ref 16.

From Figure 3(b), it can be seen that  $\beta\text{-TaO}_3$  has no intrinsic magnetic moment and exhibits an insulating character with a large direct  $E_g$  of  $3.78$  eV at the  $\Gamma$  k-point. It is found that the valence band edges are rather flat across all reciprocal space.

Similar to  $\alpha\text{-TaO}_3$ , the 2D nanosheet  $\beta'\text{-TaO}_3$  structure shows a magnetic moment of  $0.21 \mu_{\text{B}}/\text{atom}$ ; the indirect  $E_g$  is found to be  $5.31$  eV for the up-spin states, while that for the down-spin states is  $4.86$  eV (from  $\Gamma$  to R k-point), which is somewhat larger than the  $E_g$  of  $\beta\text{-TaO}_3$ . This opening of  $E_g$  for the nanosheet of  $\text{TaO}_3$  follows the same trend as  $\text{TiO}_2$  where

the nanosheet of  $\text{TiO}_2$  was also found to be approximately 0.6 eV larger than that for its parent bulk structure.<sup>48</sup> This was largely attributed to the quantum confinement effect commonly seen for low-dimensional nanomaterials. When compared to the experimentally determined optical  $E_g$  value of 5.3 eV,<sup>10</sup> our HSE06  $E_g$  value agrees fairly well. We also note that for the down-spin states, midgap states (around 1 to 3 eV) appear due to the under-coordination of the outermost oxygens in  $\beta'$ - $\text{TaO}_3$ .

**3.5. Chemical Bonding.** To understand the chemical bonding properties in the various  $\text{TaO}_3$  polyphases, we compute the ELFs (cf. eq 3) for them and present in Figures 4(a) and 4(b) the results for  $\alpha\text{-TaO}_3$  and  $\beta\text{-TaO}_3$ , respectively.

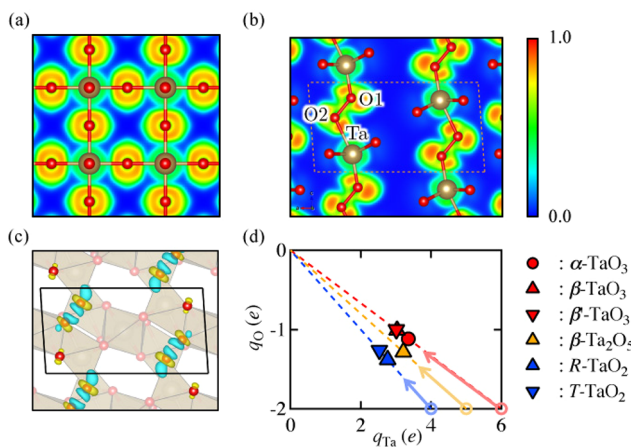


**Figure 4.** Cross section of the electron localization function (ELF) for (a)  $\alpha\text{-TaO}_3$  and (b)  $\beta\text{-TaO}_3$ . Gray and red spheres denote the Ta and O atoms, respectively, and the colored ELF scale is included next to (b). (c) The difference charge density plot for  $\beta\text{-TaO}_3$  with a 0.017 e/ $\text{\AA}^3$  isosurface value is shown; the electron charge depletion is colored cyan, while the charge accumulation is shown in yellow. (d) Calculated averaged net Bader charge of the oxygen anion ( $q_O$ ) versus the averaged net Bader charge of the tantalum cation ( $q_{\text{Ta}}$ ) in electrons (e) for  $\alpha\text{-TaO}_3$  (red circle),  $\beta\text{-TaO}_3$  (red triangle),  $\beta'\text{-TaO}_3$  (red inverse triangle),  $\beta\text{-Ta}_2\text{O}_5$  (yellow triangle),  $R\text{-TaO}_2$  (blue triangle), and  $T\text{-TaO}_2$  (blue inverse triangle).

The ELF line profiles along the Ta–O bond for the  $\text{TaO}_3$  polyphases and  $\beta\text{-Ta}_2\text{O}_5$  are shown in Figure S4(a). The concept of the ELF is numerically simple and instructive. Taking values from 0 to 1, a value of 0.5 (in green) will typically suggest covalent-type bonding while a value of 1 (in red) will imply complete localization. Likewise, a value of 0 (in blue) will indicate complete delocalization of the electron density.

In Figure 4(a), we report an isotropic symmetric distribution of the ELF for  $\alpha\text{-TaO}_3$ , with a minimum value of 0.34 at the midpoint (approximately 1 Å) between the Ta and O atoms (see Figure S4(a)). The ELF line profiles of the Ta–O bonds in  $\text{TaO}_3$  polyphases and  $\beta\text{-Ta}_2\text{O}_5$  reveal that, interestingly,  $\alpha\text{-TaO}_3$ ,  $\beta'\text{-TaO}_3$ , and  $\beta\text{-Ta}_2\text{O}_5$  share rather similar bonding features while  $\beta\text{-TaO}_3$  offers an additional ELF line profile due to additional Ta–O2 bonds (in spite of the Ta–O1 bonds which are more similar to those of the other tantalum oxides, see Figure 4(b))). The less common Ta–O2 bonds are due to the Ta atom off-center displacement in the  $\text{TaO}_6$  octahedrals in  $\beta\text{-TaO}_3$  which are not found in other Ta–O systems.

The ELF line profile is also calculated for the outermost oxygen atoms (i.e., O1–O2) for  $\beta\text{-TaO}_3$  and is plotted in Figure S4(b). Here, it is found that the ELF line profile varies

between 0.32 and 0.73, averaging about 0.5. This suggests that some form of electron sharing may occur between the outermost oxygens (i.e., O1 and O2) and, perhaps, not via the weaker van der Waals-type bonding. This then explains why the energy cost to delaminate  $\beta\text{-TaO}_3$  to form the nanosheet  $\beta'\text{-TaO}_3$  is nontrivial. This is further supported from our calculated  $\Delta\rho(\mathbf{r})$  (cf. eq 4, shown in Figure 4(c)) where electronic charge redistribution occurs via the depletion of electrons from the outermost oxygens in  $\beta\text{-TaO}_3$ .

**3.6. Atomic Charges.** As motivated by our ELF and  $\Delta\rho$  analyses, it is indeed timely to examine the actual charge state of Ta and O in  $\text{TaO}_3$ . Within the conventional “purely ionic” model, it seems completely impossible for  $\text{TaO}_3$  to exist, as the  $\text{Ta}^{6+}$  cation implies removing an additional electron completely from the 5p shell after emptying the 5d shell to donate to the  $\text{O}^{2-}$  anion. This may seem true that Ta may not be further oxidized beyond the +5 state if one considers only the formal oxidation states.

However, of late, there has been a challenge to this well-established concept of formal oxidation states, calling for a reassessment of how one defines the absolute charge state in atoms. Interesting discussions and debates have taken place between Walsh and co-workers<sup>49</sup> and Koch and co-workers,<sup>50,51</sup> representing opposite camps and schools of thought on this subject matter, on elucidating the actual charge state of Ti in the common yet technologically very important  $\text{TiO}_2$ .

While Walsh and co-workers argue that simple electron counting rules in valence chemistry should be observed, Koch and co-workers challenged and critically questioned the validity of this empirical rule.<sup>49–51</sup> Koch and co-workers then conclude that Ti may indeed have the so-called “unthinkable” +2.5 or +3 state, instead of the perceived +4 state from the “textbook” electron counting rule. In our humble opinion, this debate seems to be far from over.

Coming back to the case of  $\text{TaO}_3$ , in light of this recent discussion (or refuting) of formal oxidation states, we realize it now does not seem so unlikely that  $\text{TaO}_3$  may actually exist! To test and challenge the validity of the ionic model for Ta–O systems, we calculate the Bader charges for all Ta–O systems discussed in this work, i.e.,  $\alpha\text{-TaO}_3$ ,  $\beta\text{-TaO}_3$ ,  $\beta'\text{-TaO}_3$ ,  $R\text{-TaO}_2$ , and  $T\text{-TaO}_2$ . The corresponding Bader charge values are averaged and listed in Table 2. To further contrast our findings

**Table 2. Averaged Bader Charges for Each Atom in  $\alpha\text{-TaO}_3$ ,  $\beta\text{-TaO}_3$ ,  $\beta'\text{-TaO}_3$ ,  $R\text{-TaO}_2$ , and  $T\text{-TaO}_2$  in Units of Electrons (e)**

	$\alpha\text{-TaO}_3$	$\beta\text{-TaO}_3$	$\beta'\text{-TaO}_3$	$\beta\text{-Ta}_2\text{O}_5$	$R\text{-TaO}_2$	$T\text{-TaO}_2$
Ta	+3.35	+3.03	+3.01	+3.21	+2.76	+2.53
O	-1.12	-1.01	-1.00	-1.28	-1.38	-1.26

with the formal oxidation state model, we plot the calculated Bader charge values for Ta and O (labeled as  $q_{\text{Ta}}$  and  $q_O$ , respectively) in Figure 4(d). Here, it is clear that our calculated  $q_{\text{Ta}}$  and  $q_O$  values lie far from the expected ideal formal oxidation charge states for  $\text{TaO}_2$ ,  $\text{Ta}_2\text{O}_5$ , and  $\text{TaO}_3$ , i.e.,  $\text{Ta}^{4+}$ ,  $\text{Ta}^{5+}$ , and  $\text{Ta}^{6+}$ , respectively, with  $\text{O}^{2-}$ .

Somewhat supporting Koch’s argument, our calculated ELF,  $\Delta\rho$ , and Bader charge analyses point to the fact that the chemical bonding nature between the Ta and O atoms in the Ta–O systems is indeed not completely ionic, and thus, an ionic-covalent picture might be more appropriate. Interestingly, the Ta–O compounds discussed in this work possess very large

$E_g$  values, which again may give a false impression that these “d metal oxides” are more ionic than covalent. Arguably, the chemistry in these Ta–O compounds may, in fact, be more similar to that of ionic-covalent metal oxides with large  $E_g$  values, e.g.,  $\text{ZrO}_2$  and  $\text{HfO}_2$ .

### 3.7. Band Edge Alignment and Potential Applications.

We now turn to the calculations of band offsets by aligning the O 1s core levels for the various Ta–O compounds, in an attempt to understand how these Ta-based oxides may perform in photodevices, e.g., in polymer solar cells (PSCs). To improve the performance of PSCs, band engineering of interfacial layers, including electron transport layers (ETLs) and hole transport layers (HTLs), is critical to promote charge carrier extraction or separation by matching the electronic energy level with the electrode (or active layer).<sup>53</sup>

Conventionally, polymers such as poly(3,4-ethylene-dioxythiophene)/poly(styrene-sulfonate) (PEDOT/PSS) are used as the HTLs. However, these HTL polymers are prone to acid attack, which results in the degradation of the PSC. High work function metal oxides (e.g.,  $\text{MoO}_3$  and  $\text{WO}_3$ ), on the other hand, are more resilient and are some of the most promising candidates. A high work function is needed to ensure the transference of the excited hole from the active layer to the  $\epsilon_{\text{CMB}}$  of the metal oxide.<sup>52</sup>

To investigate if these  $\text{TaO}_3$  polyphases and  $\text{Ta}_2\text{O}_5$  can match up as HTLs in PSCs, we perform band alignment calculations using the computed IP and EA values of  $\alpha\text{-TaO}_3$ ,  $\beta\text{-TaO}_3$ ,  $\beta'\text{-TaO}_3$ , and  $\beta\text{-Ta}_2\text{O}_5$ , with respect to the vacuum level, as shown in Figure 5(a). Generally, the low IP values of

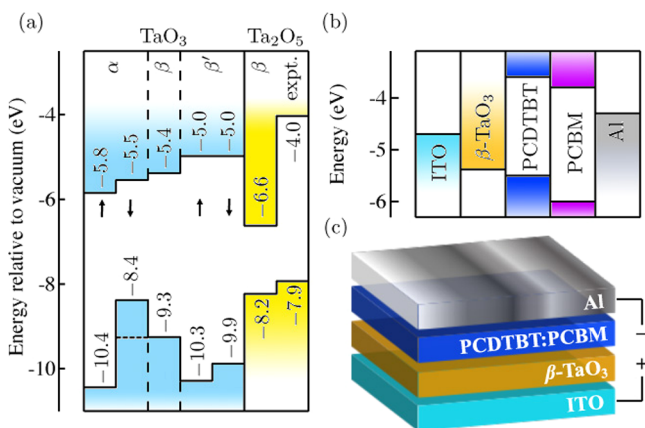


**Figure 5.** (a) Band offsets calculated for  $\alpha\text{-TaO}_3$ ,  $\beta\text{-TaO}_3$ ,  $\beta'\text{-TaO}_3$ , and  $\beta\text{-Ta}_2\text{O}_5$ . (b) Schematic band alignment diagram for polymer solar cell (PSC) applications, using Al as the cathode ( $-4.3$  eV for work function), phenyl-C61-butrylic acid methyl ester (PCBM) ( $-6.0$  and  $-3.8$  eV for LUMO and HOMO levels, respectively) and poly(*N*'-heptadecanyl-2,7-carbazole-*alt*-5,5-(4',7'-di-2-thienyl-2',1',3'-benzothiadiazole)) (PCDTBT) ( $-5.5$  and  $-3.6$  eV for LUMO and HOMO levels, respectively) as the active layers,  $\beta\text{-TaO}_3$  as the hole transfer layer (HTL) ( $-5.4$  eV for  $\epsilon_{\text{CMB}}$ ), and indium tin oxide (ITO) ( $-4.7$  eV for the work function) as the anode.<sup>52</sup> (c) Schematic model of the suggested PSC device.

TaO<sub>3</sub> are comparable with the previously reported value for the hexagonal phase of MoO<sub>3</sub>.<sup>15</sup> The variation of the  $\epsilon_{\text{VMB}}$  for the various TaO<sub>3</sub> polyphases is much larger than that of the  $\epsilon_{\text{CMB}}$ . It is notable that the  $\epsilon_{\text{VMB}}$  of  $\beta\text{-Ta}_2\text{O}_5$  matches well with the experimental IP value, but the  $\epsilon_{\text{CMB}}$  agrees less favorably (by

about  $2.6$  eV).<sup>54</sup> Of all the TaO<sub>3</sub> polyphases,  $\beta\text{-TaO}_3$  seems most promising.

Now, to compare how the IP and EA of  $\beta\text{-TaO}_3$  line up with the other components in a typical PSC, a schematic band diagram is drawn in Figure 5(b) where the band edges of the other components are taken from ref 55. The  $\epsilon_{\text{CMB}}$  and  $\epsilon_{\text{VMB}}$  of  $\beta\text{-TaO}_3$  indeed align favorably, which indicate it is very suitable as a HTL for extracting the hole to the anode (indium tin oxide (ITO)) and preventing the reverse transport back to the active layer. More specifically, the  $\epsilon_{\text{CMB}}$  of  $\beta\text{-TaO}_3$  ( $-5.4$  eV) is positioned above the IP of active organic materials ( $-6$  and  $-5.5$  eV, see Figure 5(b)) and below the work function value of ITO ( $-4.7$  eV). In addition, the  $\epsilon_{\text{VMB}}$  of  $\beta\text{-TaO}_3$  ( $-9.3$  eV) is sufficiently low such that it can also prohibit back flow from ITO to the HTL.<sup>52</sup>

## 4. CONCLUSION

In summary, using DFT calculations, we have examined the lattice parameters, energetics, and electronic properties of three TaO<sub>3</sub> polyphases, namely, cubic  $\alpha\text{-TaO}_3$ , layered  $\beta\text{-TaO}_3$ , and nanosheet  $\beta'\text{-TaO}_3$ . The most thermodynamically (as well as elastically and dynamically) stable structure is the layered  $\beta\text{-TaO}_3$ . We have also investigated the chemical bonding in these oxides and have found that they are indeed not completely ionic and exhibit a more ionic-covalent bonding. We calculated the band offsets by aligning the O 1s core levels for  $\beta\text{-TaO}_3$  and compared the band edge alignment to other components in the polymer solar cell. The IP and EA of  $\beta\text{-TaO}_3$  are found to align favorably, thus making it a very promising HTL material candidate.

## ASSOCIATED CONTENT

### Supporting Information

The Supporting Information is available free of charge on the ACS Publications website at DOI: [10.1021/acs.inorgchem.8b00578](https://doi.org/10.1021/acs.inorgchem.8b00578).

Structural parameters and the enthalpy of formation of polymorphic TaO<sub>3</sub>, TaO, TaO<sub>2</sub>, and Ta<sub>2</sub>O<sub>5</sub> phases with PBE, PBEsol, and optB88 functionals with VASP code; structural parameters and the enthalpy of formation of polymorphic TaO<sub>3</sub>, TaO, TaO<sub>2</sub>, and Ta<sub>2</sub>O<sub>5</sub> phases with PBE, PBEsol, and optB88 functionals with VASP code with other theoretical and relevant experimental values; structural parameters and the enthalpy of formation of  $\alpha$ - and  $\beta\text{-TaO}_3$  with Quantum ESPRESSO code and their computational details; calculated elastic stiffness tensors and Born mechanical stability criteria for cubic, monoclinic, and 2D crystal systems; phonon dispersion and projected phonon densities of state of TaO<sub>3</sub> phases with VASP and Quantum Espresso code; linear plot of the electron localization function (ELF) between Ta and O and between O and O for various TaO<sub>3</sub> phases; optical responses of various TaO<sub>3</sub> polyphases (PDF)

## AUTHOR INFORMATION

### Corresponding Author

\*E-mail: [aloyius.soon@yonsei.ac.kr](mailto:aloyius.soon@yonsei.ac.kr).

### ORCID

Yun-Jae Lee: [0000-0003-0181-5351](https://orcid.org/0000-0003-0181-5351)

Taehun Lee: [0000-0002-5435-5910](https://orcid.org/0000-0002-5435-5910)

Aloysius Soon: [0000-0002-6273-9324](https://orcid.org/0000-0002-6273-9324)

**Notes**

The authors declare no competing financial interest.

**ACKNOWLEDGMENTS**

We thank Y. H. Lee and U. C. Kim for fruitful discussions. We gratefully acknowledge support from the National Research and Development Program of Ministry of Science, ICT, and Future Planning (2017M3A7B4032124). Computational resources have been kindly provided by the KISTI Supercomputing Center (KSC-2017-C3-0059) and the Australian National Computational Infrastructure (NCI).

**REFERENCES**

- (1) Yu, X.; Marks, T. J.; Facchetti, A. Metal Oxides For Optoelectronic Applications. *Nat. Mater.* **2016**, *15*, 383–396.
- (2) Ma, R.; Sasaki, T. Nanosheets of Oxides and Hydroxides: Ultimate 2D Charge-Bearing Functional Crystallites. *Adv. Mater.* **2010**, *22*, 5082–5104.
- (3) Osada, M.; Sasaki, T. Exfoliated Oxide Nanosheets: New Solution to Nanoelectronics. *J. Mater. Chem.* **2009**, *19*, 2503–2511.
- (4) Nicolosi, V.; Chhowalla, M.; Kanatzidis, M. G.; Strano, M. S.; Coleman, J. N. Liquid Exfoliation of Layered Materials. *Science* **2013**, *340*, 1226419.
- (5) ten Elshof, J. E.; Yuan, H.; Gonzalez Rodriguez, P. Two-Dimensional Metal Oxide and Metal Hydroxide Nanosheets: Synthesis, Controlled Assembly and Applications in Energy Conversion and Storage. *Adv. Energy Mater.* **2016**, *6*, 1600355.
- (6) Villars, P.; Calvert, L. *Pearson's Handbook of Crystallographic Data for Intermetallic Phases*; ASM International: Materials Park, OH, 1991; Vol. 4.
- (7) Chaneliere, C.; Autran, J. L.; Devine, R. A. B.; Balland, B. Tantalum Pentoxide Thin Films for Advanced Dielectric Applications. *Mater. Sci. Eng., R* **1998**, *22*, 269.
- (8) Sahaym, U.; Norton, M. G. Advances in the Application of Nanotechnology in Enabling a 'hydrogen economy'. *J. Mater. Sci.* **2008**, *43*, 5395.
- (9) Kuzmichev, D. S.; Lebedinskii, Y. Y. Resistive Switching in MIM Structure Based on Overstoichiometric Tantalum Oxide. *Microelectron. Eng.* **2017**, *178*, 150–153.
- (10) Fukuda, K.; Nakai, I.; Ebina, Y.; Ma, R.; Sasaki, T. Colloidal Unilamellar Layers of Tantalum Oxide with Open Channels. *Inorg. Chem.* **2007**, *46*, 4787–4789.
- (11) Xu, X.; Takada, K.; Fukuda, K.; Ohnishi, T.; Akatsuka, K.; Osada, M.; Hang, B. T.; Kumagai, K.; Sekiguchi, T.; Sasaki, T. Tantalum Oxide Nanomesh As Self-standing One Nanometre Thick Electrolyte. *Energy Environ. Sci.* **2011**, *4*, 3509–3512.
- (12) Cui, Z. H.; Jiang, H. Theoretical Investigation of Ta<sub>2</sub>O<sub>5</sub>, TaON, and Ta<sub>3</sub>N<sub>5</sub>: Electronic Band Structures and Absolute Band Edges. *J. Phys. Chem. C* **2017**, *121*, 3241–3251.
- (13) Wang, F.; Di Valentin, C.; Pacchioni, G. Electronic and Structural Properties of WO<sub>3</sub>: A Systematic Hybrid DFT Study. *J. Phys. Chem. C* **2011**, *115*, 8345–8353.
- (14) Ping, Y.; Galli, G. Optimizing the Band Edges of Tungsten Trioxide for Water Oxidation: A First-principles Study. *J. Phys. Chem. C* **2014**, *118*, 6019–6028.
- (15) Yun, J.; Jang, W.; Lee, T.; Lee, Y.; Soon, A. Aligning the Band Structures of Polymorphic Molybdenum Oxides and Organic Emitters in Light-Emitting Diodes. *Phys. Rev. Appl.* **2017**, *7*, 024025.
- (16) Ravi, C.; Kaur, G.; Bharathi, A. First-principles Study of Lattice Stability of ReO<sub>3</sub>-type Hypothetical TaO<sub>3</sub>. *Comput. Mater. Sci.* **2014**, *90*, 177.
- (17) Tao, J. Z.; Sleight, A. W. Very Low Thermal Expansion in TaO<sub>2</sub>F. *J. Solid State Chem.* **2003**, *173*, 45–48.
- (18) Blöchl, P. E. Projector Augmented-Wave Method. *Phys. Rev. B: Condens. Matter Mater. Phys.* **1994**, *50*, 17953–17979.
- (19) Kresse, G.; Joubert, D. From Ultrasoft Pseudopotentials to the Projector Augmented-Wave Method. *Phys. Rev. B: Condens. Matter Mater. Phys.* **1999**, *59*, 1758–1775.
- (20) Kresse, G.; Furthmüller, J. Efficient Iterative Schemes for *Ab-Initio* Total-Energy Calculations Using a Plane-Wave Basis Set. *Phys. Rev. B: Condens. Matter Mater. Phys.* **1996**, *54*, 11169–11186.
- (21) Kresse, G.; Furthmüller, J. Efficiency of *Ab-Initio* Total Energy Calculations for Metals and Semiconductors Using a Plane-wave Basis Set. *Comput. Mater. Sci.* **1996**, *6*, 15–50.
- (22) Perdew, J. P.; Burke, K.; Ernzerhof, M. Generalized Gradient Approximation Made Simple. *Phys. Rev. Lett.* **1996**, *77*, 3865.
- (23) Perdew, J. P.; Ruzsinszky, A.; Csonka, G. I.; Vydrov, O. A.; Scuseria, G. E.; Constantin, L. A.; Zhou, X.; Burke, K. Restoring the Density-gradient Expansion for Exchange in Solids and Surfaces. *Phys. Rev. Lett.* **2008**, *100*, 136406.
- (24) Klimeš, J.; Bowler, D. R.; Michaelides, A. Chemical Accuracy For the Van Der Waals Density Functional. *J. Phys.: Condens. Matter* **2010**, *22*, 022201.
- (25) Klimeš, J.; Bowler, D. R.; Michaelides, A. Van der Waals Density Functionals Applied to Solids. *Phys. Rev. B: Condens. Matter Mater. Phys.* **2011**, *83*, 195131.
- (26) Heyd, J.; Scuseria, G. E.; Ernzerhof, M. Hybrid Functionals Based on a Screened Coulomb Potential. *J. Chem. Phys.* **2003**, *118*, 8207.
- (27) Heyd, J.; Scuseria, G. E.; Ernzerhof, M. Erratum: Hybrid Functionals Based on a Screened Coulomb Potential. *J. Chem. Phys.* **2006**, *124*, 219906.
- (28) Feller, D.; Peterson, K. A. Re-examination of Atomization Energies for the Gaussian-2 Set of Molecules. *J. Chem. Phys.* **1999**, *110*, 8384–8396.
- (29) Togo, A.; Tanaka, I. First Principles Phonon Calculations in Materials Science. *Scr. Mater.* **2015**, *108*, 1.
- (30) Mouhat, F.; Coudert, F. X. Necessary and Sufficient Elastic Stability Conditions in Various Crystal Systems. *Phys. Rev. B: Condens. Matter Mater. Phys.* **2014**, *90*, 224104.
- (31) Silvi, B.; Savin, A. Classification of Chemical Bonds Based on Topological Analysis of Electron Localization Functions. *Nature* **1994**, *371*, 683–686.
- (32) Jang, W.; Yun, J.; Lee, T.; Lee, Y.; Soon, A. Disentangling the Effects of Inter- and Intra-Octahedral Distortions on the Electronic Structure in Binary Metal Trioxides. *J. Phys. Chem. C* **2018**, *122*, 3558–3566.
- (33) Lee, T.; Lee, Y.; Jang, W.; Soon, A. Understanding the Advantage of Hexagonal WO<sub>3</sub> as an Efficient Photoanode for Solar Water Splitting: A First-Principles Perspective. *J. Mater. Chem. A* **2016**, *4*, 11498–11506.
- (34) Huang, J.; Ma, R.; Ebina, Y.; Fukuda, K.; Takada, K.; Sasaki, T. Layer-by-Layer Assembly of TaO<sub>3</sub> Nanosheet/Polycation Composite Nanostructures: Multilayer Film, Hollow Sphere, and Its Photocatalytic Activity for Hydrogen Evolution. *Chem. Mater.* **2010**, *22*, 2582–2587.
- (35) Serafin, M.; Hoppe, R. Coordination Number 5 and 6 in RbTaO<sub>3</sub>: Rb<sub>4</sub><sup>2+</sup>[Ta<sub>4</sub>O<sub>12</sub>]. *Angew. Chem.* **1978**, *90*, 387–387.
- (36) Zhu, L.; Zhou, J.; Guo, Z.; Sun, Z. Metal-Metal Bonding Stabilized Ground State Structure of Early Transition Metal Monoxide TM<sub>0</sub> (TM = Ti, Hf, V, Ta). *J. Phys. Chem. C* **2016**, *120*, 10009–10014.
- (37) Zhu, L.; Zhou, J.; Guo, Z.; Sun, Z. Realization of a Reversible Switching in TaO<sub>2</sub> Polymorphs via Peierls Distortion for Resistance Random Access Memory. *Appl. Phys. Lett.* **2015**, *106*, 091903.
- (38) Lee, S.; Kim, J.; Kim, S.; Kim, S.; Park, G. Hidden Structural Order in Orthorhombic Ta<sub>2</sub>O<sub>5</sub>. *Phys. Rev. Lett.* **2013**, *110*, 235502.
- (39) Lebedinskii, Y. Y.; Chernikova, A. G.; Markeev, A. M.; Kuzmichev, D. S. Effect of Dielectric Stoichiometry and Interface Chemical State on Band Alignment Between Tantalum Oxide and Platinum. *Appl. Phys. Lett.* **2015**, *107*, 142904.
- (40) Garg, S. P.; Krishnamurthy, N.; Awasthi, A.; Venkatraman, M. The O-Ta (Oxygen-Tantalum) System. *J. Phase Equilib.* **1996**, *17*, 63–77.
- (41) Liu, Y.; Eddie Chua, K. T.; Sum, T. C.; Gan, C. K. First-principles Study of the Lattice Dynamics of Sb<sub>2</sub>S<sub>3</sub>. *Phys. Chem. Chem. Phys.* **2014**, *16*, 345–350.

- (42) Liu, H.; Cui, W.; Ma, Y. Hybrid Functional Study Rationalizes the Simple Cubic Phase of Calcium at High Pressures. *J. Chem. Phys.* **2012**, *137*, 184502.
- (43) Baroni, S.; De Gironcoli, S.; Dal Corso, A.; Giannozzi, P. Phonons and Related Crystal Properties from Density-functional Perturbation Theory. *Rev. Mod. Phys.* **2001**, *73*, 515.
- (44) Giannozzi, P.; et al. QUANTUM ESPRESSO: a Modular and Open-source Software Project for Quantum Simulations of Materials. *J. Phys.: Condens. Matter* **2009**, *21*, 395502.
- (45) Giannozzi, P.; et al. Advanced Capabilities for Materials Modelling with Quantum ESPRESSO. *J. Phys.: Condens. Matter* **2017**, *29*, 465901.
- (46) Peng, B.; Zhang, H.; Shao, H.; Xu, Y.; Zhang, R.; Zhu, H. The Electronic, Optical, and Thermodynamic Properties of Borophene from First-principles Calculations. *J. Mater. Chem. C* **2016**, *4*, 3592–3598.
- (47) Wang, H.; Li, Q.; Gao, Y.; Miao, F.; Zhou, X. F.; Wan, X. G. Strain Effects on Borophene: Ideal Strength, Negative Possions Ratio and Phonon Instability. *New J. Phys.* **2016**, *18*, 073016.
- (48) Sakai, N.; Ebina, Y.; Takada, K.; Sasaki, T. Electronic Band Structure of Titania Semiconductor Nanosheets Revealed by Electrochemical and Photoelectrochemical Studies. *J. Am. Chem. Soc.* **2004**, *126*, 5851–5858.
- (49) Walsh, A.; Sokol, A. A.; Buckeridge, J.; Scanlon, D. O.; Catlow, C. R. A. Electron Counting in Solids: Oxidation States, Partial Charges, and Ionicity. *J. Phys. Chem. Lett.* **2017**, *8*, 2074–2075.
- (50) Koch, D.; Manzhos, S. On the Charge State of Titanium in Titanium Dioxide. *J. Phys. Chem. Lett.* **2017**, *8*, 1593–1598.
- (51) Koch, D.; Manzhos, S. Addition to “On the Charge State of Titanium in Titanium Dioxide. *J. Phys. Chem. Lett.* **2017**, *8*, 3945–3946.
- (52) Hou, F.; Su, Z.; Jin, F.; Yan, X.; Wang, L.; Zhao, H.; Zhu, J.; Chu, B.; Li, W. Efficient and Stable Planar Heterojunction Perovskite Solar Cells with an MoO<sub>3</sub>/PEDOT:PSS Hole Transporting Layer. *Nanoscale* **2015**, *7*, 9427–9432.
- (53) Chen, S.; Yu, X.; Zhang, M.; Li, J. C. Y.; Ding, L.; Shi, G.; Cao, J. A Graphene Oxide/Oxygen Deficient Molybdenum Oxide Nanosheet Bilayer as a Hole Transport Layer for Efficient Polymer Solar Cells. *J. Mater. Chem. A* **2015**, *3*, 18380–18383.
- (54) Chun, W. J.; Ishikawa, A.; Fujisawa, H.; Takata, T.; Kondo, J. N.; Hara, M.; Kawai, M.; Matsumoto, Y.; Domen, K. Conduction and Valence Band Positions of Ta<sub>2</sub>O<sub>5</sub>, TaON, and Ta<sub>3</sub>N<sub>5</sub> by UPS and Electrochemical Methods. *J. Phys. Chem. B* **2003**, *107*, 1798–1803.
- (55) Yip, H.-L.; Jen, A. K.-Y. Recent Advances in Solution-processed Interfacial Materials for Efficient and Stable Polymer Solar Cells. *Energy Environ. Sci.* **2012**, *5*, 5994–6011.

## **Supporting Information**

---

# **Over-stoichiometry in Heavy Metal Oxides: The Case of Iono-Covalent Tantalum Trioxides**

Yun-jae Lee, Taehun Lee, and Aloysius Soon\*

*Department of Materials Science and Engineering, Yonsei University, Seoul 03722, S.  
Korea*

E-mail: aloysius.soon@yonsei.ac.kr

Phone: +82-2-2123-5839

## Structure and energetics

Using the VASP code, we have tested various  $xc$  functionals to decide which one provides the most accurate (or balanced) description of the structural parameters for  $\text{TaO}_3$ . The GGA-PBE, PBESol and self-consistent nonlocal van der Waals force (vdW)-corrected optB88  $xc$  are used to perform the structural optimization for different structural configurations of  $\text{TaO}_3$  structures. In the comparison of an optimized vertical distance between the levels of upper and bottom oxygen atoms ( $d_{\text{O}-\text{O}'}$ ) of layered structure (Figure 1(c) of the main text) with that value of experiment, PBESol and optB88  $xc$  show the most good agreement within 5.30 % difference with respect to experimental value.<sup>1</sup> The computed structural properties of  $\text{TaO}_3$  with optB88  $xc$  and with PBE and PBESol  $xc$  are listed in Table S1.

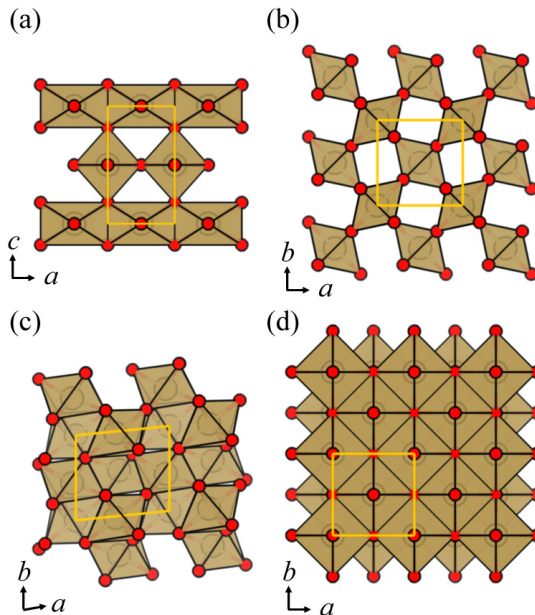


Figure S1: Crystal structures and atomic geometries of (a)  $\beta$ - $\text{Ta}_2\text{O}_5$ , (b)  $R$ - $\text{TaO}_2$ , (c)  $T$ - $\text{TaO}_2$ , and (d)  $\text{TaO}$ . The O and Ta atoms are denoted by the red and khaki colored spheres, respectively. The connecting polyhedrons are shown in khaki and the unit cells are depicted with yellow lines.

**Table S1:** Lattice properties ( $a$ ,  $b$ ,  $c$ , and  $d_{\text{O}-\text{O}'}$ , in Å and  $\alpha$ ,  $\beta$ ,  $\gamma$ , in °), space group, and energetics ( $\Delta H^f$ , in eV/atom) for various Ta-O compounds. Our theoretical values are calculated using the PBE, PBEsol and optB88  $xc$  functionals as implemented in the VASP code. Other theoretical and relevant experimental values are also listed.

	Structure	$a$	$b$	$c$	$\alpha$	$\beta$	$\gamma$	$d_{\text{O}-\text{O}'}$	Space group	$\Delta H^f$
PBE	$\alpha\text{-TaO}_3$	3.95	3.95	3.95	90	90	90	-	<i>Pm3m</i>	-2.59
	$\beta\text{-TaO}_3$	9.80	8.92	5.37	90	98.3	90	6.94	<i>C2/m</i>	-2.63
PBEsol	$\alpha\text{-TaO}_3$	3.92	3.92	3.92	90	90	90	-	<i>Pm3m</i>	-2.81
	$\beta\text{-TaO}_3$	9.70	8.81	5.28	90	97.7	90	6.92	<i>C2/m</i>	-2.87
optB88	TaO	4.50	4.50	4.50	90	90	90	-	<i>Fm-3m</i>	-1.35
	<i>R</i> -TaO <sub>2</sub>	4.98	4.98	2.89	90	90	90	-	<i>P4<sub>2</sub>/mnmm</i>	-3.16
	<i>T</i> -TaO <sub>2</sub>	4.69	5.20	5.72	90.1	87.2	95.7	-	<i>P-1</i>	-3.20
	$\beta\text{-Ta}_2\text{O}_5$	3.70	3.89	6.49	90	90	90	-	<i>Pmmm</i>	-3.10
ref.	<i>R</i> -TaO <sub>2</sub> <sup>2</sup>	4.71	4.71	3.07	90	90	90	-	<i>P4<sub>2</sub>/mnmm</i>	-
	<i>T</i> -TaO <sub>2</sub> <sup>2</sup>	4.70	5.20	5.72	90	87.3	95.7	-	<i>P-1</i>	-
	$\beta\text{-Ta}_2\text{O}_5$ <sup>3</sup>	3.67	3.86	6.43	90	90	90	-	<i>Pmmm</i>	-
	$\alpha\text{-TaO}_3$ <sup>4</sup>	3.95	3.95	3.95	90	90	90	-	<i>Pm3m</i>	-2.77
exp.	TaO <sup>5</sup>	4.43	4.43	4.43	90	90	90	-	<i>Fm-3m</i>	-
	TaO <sub>2</sub> <sup>5</sup>	4.71	4.71	3.07	90	90	90	-	<i>P4<sub>2</sub>/mnmm</i>	-
	$\beta\text{-Ta}_2\text{O}_5$ <sup>6</sup>	3.68	3.90	6.22	90	90	90	-	<i>Pmmm</i>	-
	TaO <sub>3</sub> <sup>1</sup>	9.60	8.43	7.33	90	94.5	90	6.62	<i>C2/m</i>	-
	RbTaO <sub>3</sub> <sup>7</sup>	9.85	8.51	8.14	90	94.9	90	6.62	<i>C2/m</i>	-

**Table S2:** Lattice properties ( $a$ ,  $b$ ,  $c$ , and  $d_{\text{O}-\text{O}'}$ , in Å and  $\alpha$ ,  $\beta$ ,  $\gamma$ , in  $^\circ$ ), space group, and energetics ( $\Delta H^f$ , in eV/atom) for various  $\text{TaO}_3$  polyphases. Our theoretical values are calculated using the PBE, PBESol and optB88  $xc$  functionals as implemented in the Quantum-ESPRESSO package.

	Structure	$a$	$b$	$c$	$\alpha$	$\beta$	$\gamma$	$d_{\text{O}-\text{O}'}$	Space group	$\Delta H^f$
PBE	$\alpha$ - $\text{TaO}_3$	3.94	3.94	3.94	90	90	90	-	$Pm3m$	-2.65
	$\beta$ - $\text{TaO}_3$	9.77	8.96	5.27	90	97.1	90	6.94	$C2/m$	-2.68
PBESol	$\alpha$ - $\text{TaO}_3$	3.91	3.91	3.91	90	90	90	-	$Pm3m$	-2.96
	$\beta$ - $\text{TaO}_3$	9.66	8.80	5.26	90	98.0	90	6.92	$C2/m$	-3.01
optB88	$\alpha$ - $\text{TaO}_3$	3.92	3.92	3.92	90	90	90	-	$Pm3m$	-3.45
	$\beta$ - $\text{TaO}_3$	9.73	8.84	5.34	90	99.1	90	6.92	$C2/m$	-3.49

For cross-checking, DFT calculations using periodic supercell model are also performed with the Quantum-ESPRESSO package.<sup>8</sup> Here, ultrasoft pseudopotentials were used with the plane wave kinetic energy cutoff of 50 Ry.<sup>9</sup> A  $\Gamma$ -centered  $\mathbf{k}$ -point mesh with a spacing of  $0.2 \text{ \AA}^{-1}$  is used to sample the Brillouin-zone, which is same as our detail with VASP code (as detailed in the main text). For the energetics of various tantalum oxide structures, we have tested a few semi-local approximations to the  $xc$  functional – namely that due to Perdew, Burke, and Ernzerhof (PBE)<sup>10</sup> and its revised form for solids (PBESol),<sup>11</sup> as well as the self-consistent van der Waals (vdW) corrected  $xc$  functional, optB88.<sup>12,13</sup>

## Elastic and dynamical stability

**Table S3:** Calculated elastic constants  $C_{ij}$  (in GPa) for  $\alpha\text{-TaO}_3$ ,  $\beta\text{-TaO}_3$  and  $\beta'\text{-TaO}_3$  using the optB88  $xc$  functional. Other theoretical values<sup>4</sup> are included for comparison.

	$\alpha\text{-TaO}_3$	$\beta\text{-TaO}_3$	$\beta'\text{-TaO}_3$	$\alpha\text{-TaO}_3$ <sup>4</sup>
$C_{11}$	480.1	162.1	18.5	487.6
$C_{22}$	-	115.2	19.3	-
$C_{33}$	-	133.8	-	-
$C_{44}$	35.6	11.3	6.4	34.6
$C_{55}$	-	42.6	-	-
$C_{66}$	-	20.8	-	-
$C_{12}$	47.3	43.5	4.9	52.7
$C_{13}$	-	70.0	-	-
$C_{23}$	-	52.2	-	-
$C_{15}$	-	-23.1	-	-
$C_{25}$	-	-3.8	-	-
$C_{35}$	-	-47.8	-	-
$C_{46}$	-	1.4	-	-

For  $\alpha\text{-TaO}_3$  or cubic system, the stability criteria is as follow,

$$C_{11} + 2C_{12} > 0, C_{44} > 0, C_{11} - C_{12} > 0 \quad (1)$$

For  $\beta\text{-TaO}_3$  or monoclinic system,

$$C_{11}, C_{22}, C_{33}, C_{44}, C_{55}, C_{66} > 0, \quad (2)$$

$$[C_{11} + C_{22} + C_{33} + 2(C_{12} + C_{13} + C_{23})] > 0,$$

$$(C_{33}C_{55} - C_{35}^2) > 0, (C_{44}C_{66} - C_{46}^2) > 0,$$

$$(C_{22} + C_{33} - 2C_{23}) > 0,$$

$$[C_{22}(C_{33}C_{55} - C_{35}^2) + 2C_{23}C_{25}C_{35} - C_{23}^2C_{55} - C_{25}^2C_{33}] > 0,$$

$$2[C_{15}C_{25}(C_{33}C_{12} - C_{13}C_{23}) + C_{15}C_{35}(C_{22}C_{13} - C_{12}C_{23}) + C_{25}C_{35}(C_{11}C_{23} - C_{12}C_{13})]$$

$$-[C_{15}^2(C_{22}C_{33} - C_{23}^2) + C_{25}^2(C_{11}C_{33} - C_{13}^2) + C_{35}^2(C_{11}C_{22} - C_{12}^2)] + gC_{55} > 0$$

$$(g = C_{11}C_{22}C_{33} - C_{11}C_{23}^2 - C_{22}C_{13}^2 - C_{33}C_{12}^2 + 2C_{12}C_{13}C_{23})$$

For  $\beta'$ -TaO<sub>3</sub> or 2D system,

$$C_{11}C_{22} - C_{12}^2 > 0, C_{11}, C_{22}, C_{44} > 0 \quad (3)$$

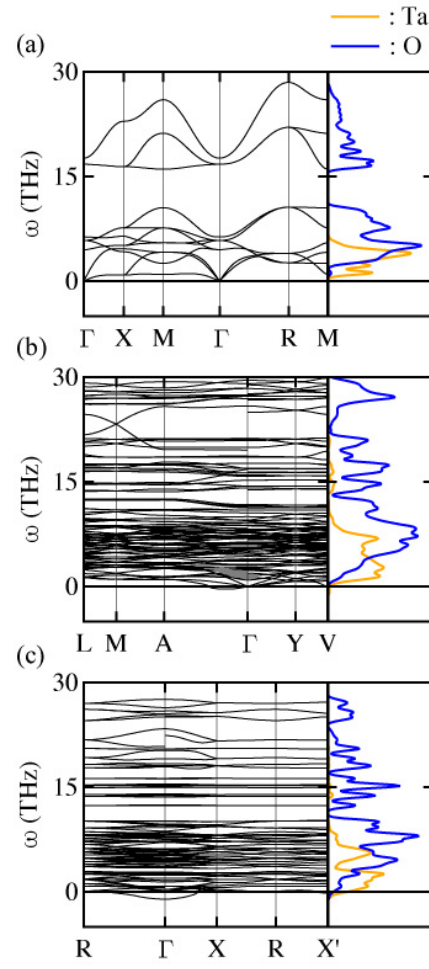


Figure S2: Phonon dispersion plots (as shown on the left panel) with the corresponding projected phonon density-of-states (as shown on the right panel) for (a)  $\alpha\text{-TaO}_3$ , (b)  $\beta\text{-TaO}_3$ , and (c)  $\beta'\text{-TaO}_3$ . These are calculated using the optB88  $xc$  functional as implemented in the VASP code.

For cross-checking, density functional perturbation theory (DFPT) calculations using periodic supercell model with the Quantum-ESPRESSO package<sup>8</sup> are also performed. For the lattice dynamics with  $\beta$ -TaO<sub>3</sub>, phonon frequencies are calculated within the DFPT framework.  $2 \times 2 \times 3$   $\mathbf{q}$ -point grids are used for the  $\beta$ -TaO<sub>3</sub>. We also consider the LO-TO splitting in our final phonon dispersion plot as shown in Figure S3.

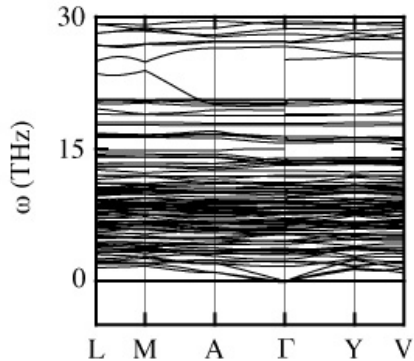


Figure S3: Phonon dispersion plot of  $\beta$ -TaO<sub>3</sub> calculated using the optB88 *xc* functional as implemented in the Quantum-ESPRESSO package.

## Chemical bonding analysis

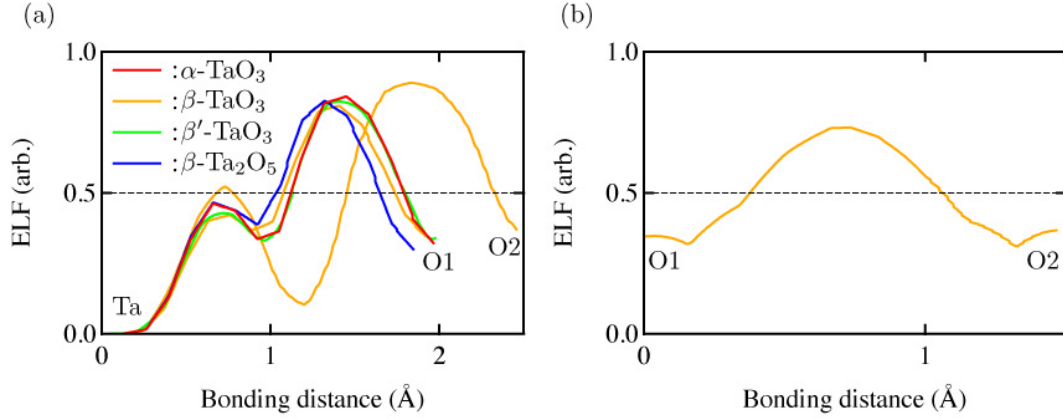


Figure S4: Electron localization function (ELF) line profiles for  $\alpha\text{-TaO}_3$  (red line),  $\beta\text{-TaO}_3$  (yellow line) to 2 different oxygen (namely O1 and O2 in Fig. 4),  $\beta'\text{-TaO}_3$  (green line) and  $\beta\text{-Ta}_2\text{O}_5$  (blue line), and (b) between O1 and O2 for  $\beta\text{-TaO}_3$ . Dotted horizontal line located at the 0.5 of ELF value indicates the covalent nature.

## Optical responses

Using the independent-particle approximation (IPA) approach,<sup>14</sup> we calculate the optical responses for the polymorphs of  $\text{TaO}_3$  studied in this work. Despite of neglecting the excitonic and local-field effects, the IPA approach seems rather successful in providing a qualitative picture of the dielectric properties of many metal oxides.<sup>15–17</sup>

Briefly, for the interband transitions, the imaginary part of the dielectric function,  $\epsilon_2^{\alpha\beta}(\omega)$  is obtained upon the summation over the empty states as follows,

$$\epsilon_2^{\alpha\beta}(\omega) = \frac{4\pi^2 e^2}{\Omega} \lim_{q \rightarrow 0} \frac{1}{q^2} \sum_{c,v,\mathbf{k}} 2\omega_{\mathbf{k}} \delta(\epsilon_{c\mathbf{k}} - \epsilon_{v\mathbf{k}} - \omega) \times \langle u_{c\mathbf{k} + \mathbf{e}_{\alpha}q} | u_{v\mathbf{k}} \rangle \langle u_{c\mathbf{k} + \mathbf{e}_{\beta}q} | u_{v\mathbf{k}} \rangle^* , \quad (4)$$

where  $\Omega$ ,  $q$ ,  $c$ ,  $v$ ,  $\alpha$ , and  $\beta$  are the volume of the unit cell, the Bloch vector of incident wave, the states in the conduction bands, the states in the valence bands, and two Cartesian factors, respectively. Also, the periodic part of the Kohn-Sham orbitals ( $\psi_i^{\mathbf{k}}(\mathbf{r})$ ) at the  $\mathbf{k}$ -point,  $\mathbf{k}$  is represented as  $u_{c\mathbf{k}} = e^{-i\mathbf{k}\cdot\mathbf{r}} \psi_i^{\mathbf{k}}(\mathbf{r})$ . The real part of dielectric function,  $\epsilon_1^{\alpha\beta}(\omega)$  is

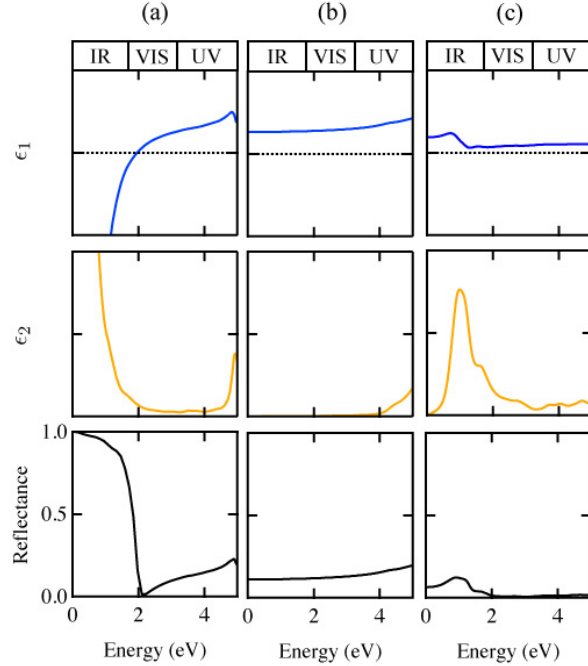


Figure S5: HSE06 computed the real and imaginary part of the dielectric function ( $\epsilon_1$ ,  $\epsilon_2$ ) with Drude-like corrections and the reflectance ( $R$ ) with IPA for (a)  $\alpha$ -TaO<sub>3</sub>, (b)  $\beta$ -TaO<sub>3</sub> and (c)  $\beta'$ -TaO<sub>3</sub>.

then derived via the Kramers-Kronig transformation, yielding

$$\epsilon_1^{\alpha\beta}(\omega) = 1 + \frac{2}{\pi} P \int_0^\infty \frac{\epsilon_2^{\alpha\beta}(\omega') \omega'}{\omega'^2 - \omega^2} d\omega' \quad . \quad (5)$$

For the metallic intraband transitions, we add a Drude-like correction term to both the imaginary and real parts of dielectric functions, following Reference 18,

$$\epsilon_2^{\text{Drude}}(\omega) = \frac{\Gamma \omega^2}{\omega(\omega^2 + \Gamma^2)} \quad , \quad (6)$$

and

$$\epsilon_1^{\text{Drude}}(\omega) = 1 - \frac{\omega^2}{\omega(\omega^2 + \Gamma^2)} \quad , \quad (7)$$

where  $\Gamma$  is taken as the lifetime broadening in the Drude model. Here, we adopt a lifetime broadening value of 0.1 eV which is commonly used for most elemental metals.<sup>19</sup>

From the Drude-corrected total dielectric function, we compute and obtain the refractive

index ( $n$ ), the extinction coefficient ( $k$ ) and finally, the reflectance ( $R$ ) from,

$$n = \frac{\sqrt{\epsilon_1 + \sqrt{\epsilon_1^2 + \epsilon_2^2}}}{\sqrt{2}} , \quad (8)$$

$$k = \frac{\sqrt{-\epsilon_1 + \sqrt{\epsilon_1^2 + \epsilon_2^2}}}{\sqrt{2}} , \quad (9)$$

and

$$R = \frac{(n - 1)^2 + k^2}{(n + 1)^2 + k^2} . \quad (10)$$

## References

- (1) Fukuda, K.; Nakai, I.; Ebina, Y.; Ma, R.; Sasaki, T. Colloidal Unilamellar Layers of Tantalum Oxide with Open Channels. *Inorg. Chem.* **2007**, *46*, 478.
- (2) Zhu, L.; Zhou, J.; Guo, Z.; Sun, Z. Realization of a Reversible Switching in TaO<sub>2</sub> Polymorphs via Peierls Distortion for Resistance Random Access Memory. *Appl. Phys. Lett.* **2015**, *106*, 091903.
- (3) Cui, Z. H.; Jiang, H. Theoretical Investigation of Ta<sub>2</sub>O<sub>5</sub>, TaON, and Ta<sub>3</sub>N<sub>5</sub>: Electronic Band Structures and Absolute Band Edges. *J. Phys. Chem. C* **2017**, *121*, 3241–3251.
- (4) Ravi, C.; Kaur, G.; Bharathi, A. First-principles Study of Lattice Stability of ReO<sub>3</sub>-type Hypothetical TaO<sub>3</sub>. *Comput. Mat. Sci.* **2014**, *90*, 177.
- (5) Schönberg, N. An X-Ray Investigation of the Tantalum-Oxygen System. *Acta Chem. Scand.* **1954**, *8*, 240–245.
- (6) Aleshina, L. A.; Loginova, S. V. Rietveld Analysis of X-ray Diffraction Pattern from  $\beta$ -Ta<sub>2</sub>O<sub>5</sub> Oxide. *Crystallogr. Rep.* **2002**, *47*, 415–419.

- (7) Serafin, M.; Hopper, R. Coordination Number 5 and 6 in RbTaO<sub>3</sub>: Rb<sub>4</sub><sup>2</sup>[Ta<sub>4</sub>O<sub>12</sub>]. *Angew. Chem.* **1978**, *90*, 387–387.
- (8) Giannozzi, P.; Baroni, S.; Bonini, N.; Calandra, M.; Car, R.; Cavazzoni, C.; Ceresoli, D.; Chiarotti, G. L.; Cococcioni, M.; Dabo, I. et al. QUANTUM ESPRESSO: a Modular and Open-source Software Project for Quantum Simulations of Materials. *J. Phys. Condens. Matter* **2009**, *21*, 395502.
- (9) Vanderbilt, D. Soft Self-consistent Pseudopotentials in a Generalized Eigenvalue Formalism. *Phys. Rev. B* **1990**, *41*, 7892–7895.
- (10) Perdew, J. P.; Burke, K.; Ernzerhof, M. Generalized Gradient Approximation Made Simple. *Phys. Rev. Lett.* **1996**, *77*, 3865.
- (11) Perdew, J. P.; Ruzsinszky, A.; Csonka, G. I.; Vydrov, O. A.; Scuseria, G. E.; Constantin, L. A.; Zhou, X.; Burke, K. Restoring the Density-gradient Expansion for Exchange in Solids and Surfaces. *Phys. Rev. Lett.* **2008**, *100*, 136406.
- (12) Klimeš, J.; Bowler, D. R.; Michaelides, A. Chemical Accuracy For the Van Der Waals Density Functional. *J. Phys.: Condens. Matter* **2010**, *22*, 022201.
- (13) Klimeš, J.; Bowler, D. R.; Michaelides, A. Van der Waals Density Functionals Applied to Solids. *Phys. Rev. B* **2011**, *83*, 195131.
- (14) Gajdos, M.; Hummer, K.; Kresse, G.; Furthmüller, J.; Bechstedt, F. Linear Optical Properties in the Projector-augmented Wave Methodology. *Phys. Rev. B* **2006**, *73*, 045112.
- (15) Gavrilenko, V. I.; Bechstedt, F. Local-field and exchange-correlation effects in optical spectra of semiconductors. *Phys. Rev. B* **1996**, *54*, 13416–13419.
- (16) Walsh, A.; Yan, Y.; Huda, M. N.; Al-Jassim, M. M.; Wei, S.-H. Band Edge Electronic

Structure of BiVO<sub>4</sub>: Elucidating the Role of the Bi s and V d Orbitals. *Chem. Mater.* **2009**, *21*, 547–551.

- (17) Lee, Y.; Lee, T.; Jang, W.; Soon, A. Unraveling The Intercalation Chemistry Of Hexagonal Tungsten Bronze And Its Optical Responses. *Chem. Mater.* **2016**, *28*, 4528–4535.
- (18) Lashgari, H.; Abolhassani, M. R.; Boochani, A.; Elahi, S. M.; Khodadadi, J. Electronic and Optical Properties of 2D Graphene-like Compounds Titanium Carbides and Nitrides: DFT Calculations. *Solid State Commun.* **2014**, *195*, 61–69.
- (19) Werner, W. S. M.; Glantschnig, K.; Ambrosch-Draxl, C. Optical Constants and Inelastic Electron-Scattering Data for 17 Elemental Metals. *J. Phys. Chem. Ref. Data* **2009**, *38*, 1013–1092.